Roadway to self-healing highways with integrated wireless electric vehicle charging and sustainable energy harvesting technologies

Prasanth, Venugopal; Shekhar, Aditya; Visser, Erwin; Scheele, Natalia; Chandra Mouli, Gautham Ram; Bauer, Pavol; Silvester, Sacha

DOI
10.1016/j.apenergy.2017.12.108

Publication date
2018

Document Version
Final published version

Published in
Applied Energy

Citation (APA)
Prasanth, V., Shekhar, A., Visser, E., Scheele, N., Chandra Mouli, G. R., Bauer, P., & Silvester, S. (2018). Roadway to self-healing highways with integrated wireless electric vehicle charging and sustainable energy harvesting technologies. *Applied Energy*, *212*, 1226-1239. https://doi.org/10.1016/j.apenergy.2017.12.108

Applied Energy 212 (2018) 1226–1239

Contents lists available at ScienceDirect

Applied Energy

journal homepage: www.elsevier.com/locate/apenergy

Roadway to self-healing highways with integrated wireless electric vehicle charging and sustainable energy harvesting technologies

Prasanth Venugopal*, Aditya Shekhar, Erwin Visser, Natalia Scheele, Gautham Ram Chandra Mouli, Pavol Bauer, Sacha Silvester

Delft University of Technology, Mekelweg 04, 2628 CD, Delft, The Netherlands

HIGHLIGHTS

- Imminent combination of roadway technologies creates opportunities and challenges.
- Sectional roads and mosaic integration create exciting combinational possibilities.
- Nissan LEAF completing its A12 highway trip with 30.3% on-road contactless coverage.

GRAPHICAL ABSTRACT

ARTICLE INFO

Keywords:
Contactless power transfer
Electric vehicles
Green energy
Inductive healing
IPT
Renewable energy
Self-healing roads

ABSTRACT

Development of electric mobility and sustainable energy result in new technologies such as contactless electric vehicle charging and roadway energy harvesting methods, but also self-healing asphalt roads. By combining these technologies a new concept of Future Sustainable Roads for Electric Mobility is created and presented in the paper. This paper bridges the gap created by these unilateral technology developments using a multi-disciplinary approach including placing cautions when necessary and suggesting viable alternatives for optimal utilization of these energy transfer and conversion techniques. Through theoretical analysis, simulations, and tests on lab-scale experimental prototypes, the impact of our proposal is showcased. Thermal and loss models are developed for self-healing asphalt. Also, integration study of solar roads and contactless charging is performed. Applying the insight gained from the results, it is discussed how some challenges also pave a way towards interesting opportunities, for instance, infrastructure sharing for material use optimization and efficient mosaic integration. Finally, an economic viability case study is presented for a future Dutch highway with such newly emerging components.

1. Introduction

Electric mobility will reduce the CO_2 footprint, pollution level and help combat anthropogenic climate change [1]. A sustainable balance is thus struck between limited resources and socio-environmental demands. EVs can be further categorised as Hybrid Electric Vehicle (HEV), Plug-in Hybrid Electric Vehicle (PHEV), Range Extender Electric Vehicle (REX) and Battery Electric Vehicle (BEV) [2]. However, only BEVs are ZEVs (zero emission vehicles) at the point of use considering the dependence of fossil fuels in the other forms of EVs [2]. The low

* Corresponding author.
E-mail address: v.prasanth@tudelft.nl (P. Venugopal).

https://doi.org/10.1016/j.apenergy.2017.12.108
Received 28 September 2017; Received in revised form 28 December 2017; Accepted 30 December 2017
Available online 08 January 2018

Nomenclature

$[\frac{dT}{dt}]$	heating rate, K s^{-1}
$[\rho]$	volumetric density, kg m^{-3}
$[C_p]$	specific heat capacity, J kg^{-1} K−1
$[q]$	volume related power density, W m^{-3}.
$[W]$	wind velocity, m s^{-1}
$[k_{a/c}]$	thermal conductivity asphalt/concrete, W m^{-1} K^{-1}
h_c	convective heat transfer coefficient, W m^{-2} K^{-1}
$[R_{a/c}]$	thermal resistance of asphalt/concrete, K W^{-1}
$[Q_{in}]$	heat input, W
$[A]$	area, m^2
$[L_1,L_2,M]$	self and mutual inductances, H
$[S_{out,max}]$	uncompensated power transfer, V A
$[V_{out,oc}]$	open circuited voltage, V
$[I_{out,sc}]$	short circuited current, A
$[P_{in,max},P_{out,max}]$	input/output power, W
$[\omega]$	angular frequency, radian/s
$[R_1,R_2,R_M]$	resistance of primary, secondary and due to combined field, Ω
$[N_{primary},N_{pickup}]$	number of turns primary, pickup, –
$[k]$	magnetic coupling coefficient, –

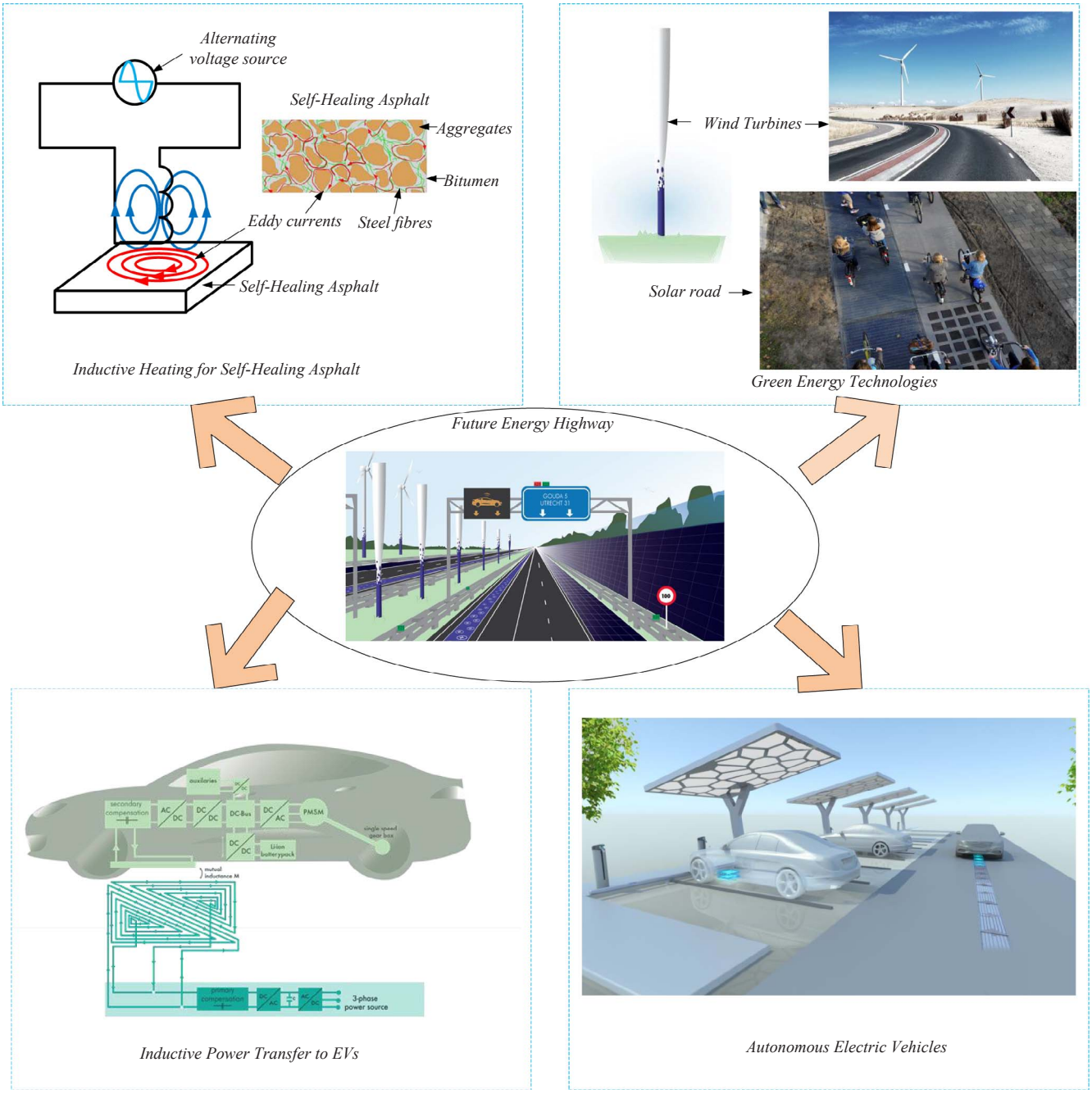

Fig. 1. Future energy highway integrating inductive coils for both inductive power transfer and induction heating, with green energy technologies for (autonomous) electric mobility.

carbon impact of EVs will be possible only if electricity is generated from sustainable sources.

Among EU countries, the Netherlands is one of the front-runners in terms of sales of EVs in 2014 [3]. It is expected that by 2020, the Netherlands will add 200,000 EVs to its roads [4]. Such a monumental transition would add pressure to infrastructure that needs to upgrade, enabling a seamless flow of EVs. Range anxiety, optimization of size and health of battery storage and utilization of sustainable energy sources in mobility are important challenges for large-scale EV deployment. Emerging technologies that tackle these challenges with a focus on roadway infrastructure - inductive charging, inductive healing asphalt and, highway-based renewable energy sources are depicted in Fig. 1. These technologies are integrated together in a combined sustainable roadway setting. Each of these technologies that are traditionally studied individually, all expecting to impact EV technology in the highway is introduced in the following paragraphs.

1.1. Wireless inductive charging of electric vehicles

IPT uses alternating magnetic fields as a mode of power transfer from one conductive circuit to another. A small band of frequency around 85 kHz (81.39–90 kHz) is being allocated for light EV IPT wireless charging for four power classes (3.7, 7.7, 11, 22 kW) [5,6]. The alternating field thus produced, links with the on-vehicle pick-up pad, thereby enabling wireless power transfer. However, the charge-pads are typically placed 10–15 cm apart which creates a large air-gap and hence a large reluctance path. Therefore, to achieve high power transfer at adequate efficiency, capacitive compensation is necessary with well-designed magnetics to curtail power reduction during misalignment [7–9].

Charge pads consisting of coils wound in several shapes, e.g., circular, rectangular, square, etc. are presently applied to IPT systems [10,11]. Coil shapes have an impact on the range of power transfer and misalignment behavior [12]. Among the various geometries, circular has the best coupling at the best-aligned point but it tends to decay faster with misalignment [13]. However, rectangular coils tend to extend the range better despite having a lower coupling at the best-aligned point [13]. Recent research has focused upon multi-coil pads as a solution to the extension of power transfer to larger lateral/longitudinal distances. Some examples of multi-coil charge-pads include Double D (DD), Double D Quadrature (DDQ) and bipolar [14,15].

There are three developments in wireless power for EV charging. They are stationary charging, semi-dynamic charging and on-road/dynamic charging. In case of stationary/static charging, parking lots can be upgraded to charging EVs comfortably without handling any HV charging cable with charge-pads. Semi-dynamic charging can be useful to deliver energy back to the battery during an opportune stop moment during a trip or during slow-moving instances e.g.: stop lights, taxi-ranks, etc. [16]. Dynamic charging can enhance battery life by charging with small packets of energy while nullifying range anxiety in long trips due to limited battery size. Dynamic charging as researched in [17], concludes that for an EV with a battery of 24 kW h, 500 km range can be achieved by IPT system of 25 kW with 40% road coverage. In a related study in California, the combination of dynamic and static charging is shown as cost-effective compared to gasoline vehicles fuelled at "$"2.50 and "$"4 per gallon [18]. In addition, it is shown that the on-road wireless charging can be used to power the EVs at stop lights in a semi-dynamic fashion in [19]. Also, several companies and research labs like Qualcomm Halo, Bombardier, Oak Ridge National Laboratory (ORNL), On-Line Electric Vehicles (OLEV) of Korea, etc. are building market-ready charge-pads for electric vehicles charging using IPT [9,20].

1.2. Inductive Self-Healing Asphalt (IHA)

Roads made with porous asphalt concrete has advantages over dense graded asphalt concrete with respect to noise reduction and water drainage. However, the porous structure does not benefit from the durability of asphalt and will cause premature raveling of the road [21]. Asphalt concrete is a self-healing material [22]. Micro cracks are formed in the material when it is exposed to a sufficiently large stress or strain. The self-healing process will start after the load that generated the damage has been removed. The diffusion of molecules from one face of crack to another and by rearrangement of the molecules within, the bulk of the material will be repaired and regain its strength [23].

The practical problem to heal roads is that the self-healing process at ambient temperature is too slow in between periods of no stress. The healing rate of the asphalt concrete will increase at higher temperatures [24]. Heated asphalt can achieve significant amounts of healing after a resting period of 3–6 h, depending on the asphalt mixture used and the damage that is present before the heating [25]. Therefore, a heating system in the road enables the asphalt to use its self-healing properties in a time period where the traffic circulation can be interrupted shortly.

The heating can be done using different methods, but induction heating is preferred over other methods because it does not contaminate the asphalt, can provide a good distribution of the heating power inside the asphalt and it is possible to properly control the amount of heat generated [25,26]. For the asphalt to be heated by means of induction, it first needs to be conductive. Thus, eddy currents are induced in the asphalt by mixing additives in the asphalt, like graphite or steel wool. Asphalt which is treated with such additives is referred to as inductive healing asphalt (IHA). The most effective form of IHA researched in [27] consists of an equal distribution of 3.2,6.4, and 9.5 mm of grade 00 steel wool. This porous asphalt concrete when heated to 85 °C and rested for a period of 3–6 h could recover 70–85% of their original strength [27].

1.3. In-situ renewable energy generation and Solar Roads (SR)

Solar energy based charging of PHEVs to reduce their carbon footprint, is introduced in [28]. Renewable energy based highways have been proposed in [29] with energy generated from the renewable micro-grid supplied to a roadway and signal lighting system, excess energy being stored in batteries. As an extension to charging EVs, solar energy and wind energy are considered for utilization in the highways of Netherlands in [30]. Also, such microgrids have been optimized for supply and demand optimization using cyber physical networks in smart buildings in [31]. Such a local utilization of renewable energy, results in lower transmission and distribution loss, savings due to reduced costs of renewable energy sources and range enhancement of EVs on wireless charging [32].

Solar roads is a Dutch innovation that consists of prefabricated concrete modules with solar cells laid on the ground with a layer of tempered glass that is translucent to light [33,34]. Crystalline silicon solar cells then convert the energy contained in photons to electricity. The maximum module efficiency attained by this technology is 9.69%. In this paper, solar roads are selected as the PV technology for implementation because of its easy installation and load-bearing capabilities on the road with less maintenance [33].

Wind energy technologies for this study include a conventional wind turbine of 2 MW and a micro-turbine based disruptive technology – 4 kW Bladeless vortex. Bladeless vortex is a Spanish start-up that produces oscillating cylindrical wind harvesters without blades that harness the *vorticity* of wind. The structure is made of fibre glass and carbon fibre [35] and uses the shear force of the wind that when falling onto the structure creates *eddies* [36]. This reciprocation is converted into electrical energy by cutting a magnetic field produced by magnets in the base.

1.4. Research objectives

In the literature survey as presented before, energy conversion (harvesting and transfer) techniques for highways including inductive

power transfer, solar roads, and self-healing asphalt are all studied in isolation. Thus, evidence of each technology being researched and improved individually is rampant. However, a collision of these roadway technologies that is both imminent and important presents a lacuna in the research community due to the absence of published work. Thus, bridging this gap by studying integration interdependencies is an important outcome of this paper. This testifies to the novelty of the work by providing evidence based implementation pathways for a combined energy conversion roadway. A recent paper studying a hybrid solar road and soil-regenerator to improve energy efficiency (between 48.42% and 66.58%) of harvesting by concurrently producing electrical and thermal energy is presented in [37].

In this light and as evidenced by the work in [37,38], it is of utmost importance to study various technologies in a hybrid, multi-disciplinary format. This way, it is possible to affirm the consequences of integration, raise important challenges and even invent ways to make them compatible and improve performance. Thus, the main goals of this paper is established by the following research objectives:

- Determining the required power density by proposing an appropriate thermal model using finite element and analytical techniques to ensure adequate performance of inductively heated asphalt.
- Identifying the interdependencies and system parameters in the combination of independently developed inductive healing and inductive power transfer technologies. This study is performed by proposing a new circuit model, extracting parameters using finite element modelling and measuring the frequency dependent losses in the asphalt sample. Finally, the performance consequence of this integration is highlighted.
- Estimating the performance in integrating wireless EV charging with energy harvesting PV technology. This is performed by measuring and modelling the mutual inductance variation using finite element studies.
- The viable alternatives from the individual technology integration as studied previously is used to design an energy conversion technology based highway. A case study based on the A12 motorway in the Netherlands is used as a real-life use case for this implementation. Such a highway is integrated with on-road dynamic wireless charging and attaining energy neutrality using energy resources like solar road, wind turbine and vortex.

2. Combining self-healing roads with IPT

Induction coils used in both self-healing roads and IPT systems is a shared infrastructure and can be utilized for both inductive power transfer and induction healing. Firstly, it is important to compute the power density required for healing a given area of self-healing asphalt. Also, the combination of these two distinct technologies bring with it various challenges and advantages. These are studied using FEM analysis as well as using lab-scale experiments.

2.1. Thermal modelling of self-healing roads

If a homogeneous asphalt sample is required to be heated from 10 °C to 80 °C in 10 min then the desired heating rate is $\frac{dT}{dt} = 0.133\ \mathrm{K\ s^{-1}}$. The density of the asphalt is approximately $\rho = 1950\ \mathrm{kg\ m^{-3}}$ and the specific heat capacity is $C_p = 920\ \mathrm{J\ kg^{-1}\ K^{-1}}$. Therefore the required power density is

$$q = \rho C_p \frac{dT}{dt} = 1950 \times 920 \times 0.133 = 233\ \mathrm{kW\ m^{-3}}. \quad (1)$$

This is a large power requirement but with limited utilization (once in 4–5 years). Thus, during healing, IPT system can transfer full/partial healing with the rest from external induction coils (currently only external heating is used).

A FEM analysis is performed to compare the estimated rise in temperature with the case when there are conduction and convection losses. The set-up used is shown in Figs. 2 and 3. In the Netherlands, the asphalt layer thickness varies from a minimum thickness of 50 mm, this is different from the US where the choice of 20 mm is preferred [39]. The larger thickness is attributed to water storage capacity requirements specific to Netherlands [39]. The simulation is performed on a solid slab of asphalt that has a size of 1 m × 1 m × 0.05 m. The slab is surrounded by a concrete hemisphere with a radius of 2 m. The choice of the hemisphere is due to ease of application of boundary conditions - conduction physics to the base concrete and convection above. The material parameters that are used are listed in Table 1. The initial temperature of the setup is 10 °C for all objects. On the spherical boundary of the hemisphere, a constant temperature boundary condition of 10 °C is applied. On the entire flat surface a convective heat flux is specified. The convective heat transfer coefficient h_c is approximated with the formula

$$h_c = 7.4 + 6.39 \times W^{0.75}, \quad (2)$$

where W is the wind velocity at 2 m above the ground. For a wind velocity of $7\ \mathrm{m\ s^{-1}}$ the thermal convection coefficient is $h_c = 34.9\ \mathrm{W\ m^{-2}\ K^{-1}}$. The heat source is defined to be homogeneously distributed through the asphalt with a value of $233\ \mathrm{kW\ m^{-3}}$.

The simulation is performed to calculate the temperature transient in the asphalt for the first 30 min of the heating. The temperature is evaluated at three points that are horizontally in the center of the asphalt. The vertical positions are the bottom, where the contact with the concrete is made, in the center and at the top, where the contact with the air is. The temperature transient of the three points is shown in the plot of Fig. 4. It can be seen that the center of the asphalt is heated to 80 °C in 620 m, which is very close to the expected 600 m. The top section is heated a bit slower, and takes 940 m to reach the desired temperature. This difference is due to the heat that is lost through the outgoing heat flux of the convection. The bottom part is heated the slowest, because of the conductive losses to the concrete surrounding the asphalt. It takes 1425 m for the bottom part to be heated to a temperature of 80 °C. In a real system the heat source will however not be distributed homogeneously through the whole material. The power dissipated in the asphalt will be higher at the locations that are closer to the coils, because the flux densities will be higher in those regions. If the coils are located underneath the asphalt, this would mean that the heat source near the bottom is higher, which will make the temperature distribution through the asphalt more constant. Inductive healing of the asphalt is expected to be necessary once every 4–5 years. This makes it possible to carefully plan the moment at which the induction heating is applied. In the summer, when the initial temperature is higher and the wind velocity is minimal a better temperature distribution can be achieved.

However, repeated heating of IHA can lead to leakage of bitumen and raveling of the top layer. To estimate this, consider a piece of road of 1 m × 1 m. The thickness x_a of the IHA layer is 0.05 m and underneath the top layer, there is a layer of concrete with a thickness x_c of 0.5 m. A heat source Q_{in} uniformly distributed in the IHA layer is

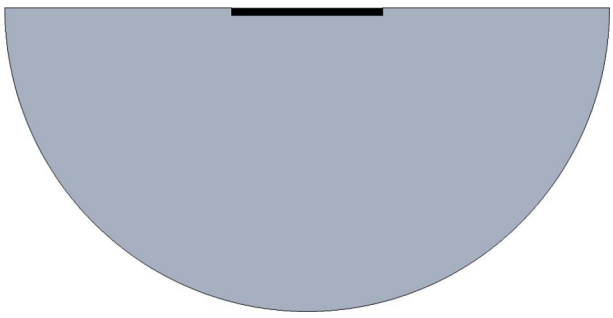

Fig. 2. Cross section of the setup.

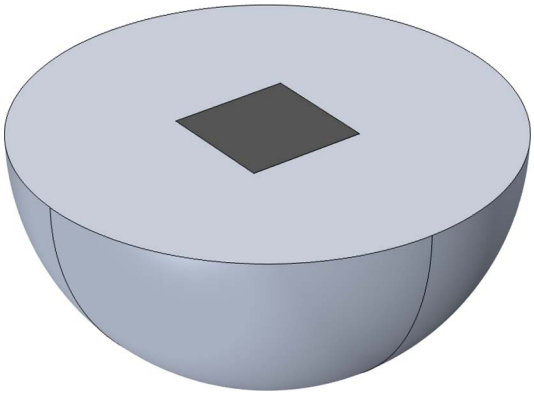

Fig. 3. Overview of the setup.

Table 1
Material parameters used for the thermal simulation.

Material	Density	Specific heat capacity	Thermal conductivity
Asphalt	1950 kg m^{-3}	920 J kg^{-1} K^{-1}	1.8 W m^{-1}
Concrete	2300 kg m^{-3}	880 J kg^{-1} K^{-1}	0.9 W m^{-1}

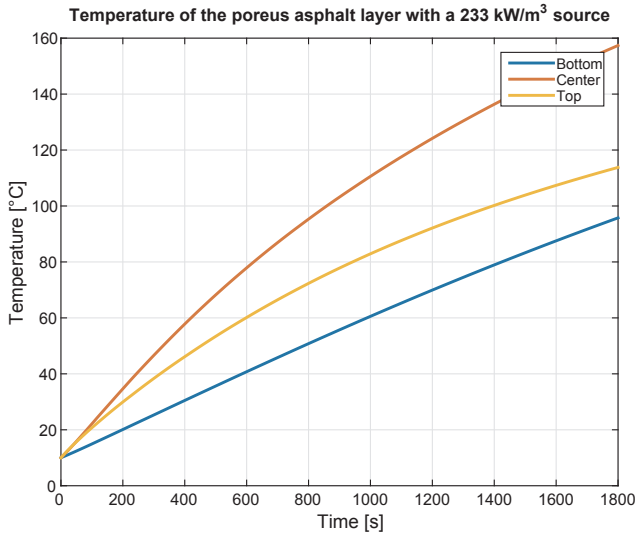

Fig. 4. Plot of the temperatures of the asphalt.

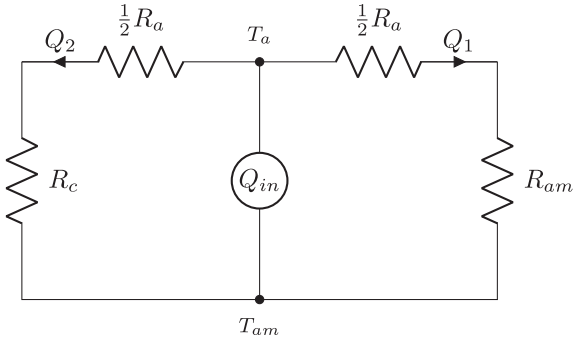

Fig. 5. Thermal circuit describing the steady-state temperatures of a highway that is considered to be a combination of a top layer of IHA and bottom layer of concrete.

considered. The steady state thermal behavior can be described using a thermal circuit as shown in Fig. 5. The thermal resistances of the asphalt and the concrete can be calculated using the respective thickness, the thermal conductivity $k_a = 1.8\ \mathrm{W\,m^{-1}}$,$k_c = 0.9\ \mathrm{W\,m^{-1}\,K^{-1}}$ and the area A as

$$R_a = \frac{x_a}{Ak_a}$$
$$R_c = \frac{x_c}{Ak_c} \tag{3}$$

The thermal resistance from asphalt to concrete is approximated to be one half of the total resistance of the asphalt, because the heat source is distributed uniformly. The bottom of the concrete is assumed to have a constant temperature equal to the ambient temperature. There is also a thermal resistance R_{am} from the top of asphalt to ambient, related to the convection coefficient h_c and area A as

$$R_{am} = \frac{1}{Ah_c} \tag{4}$$

The expression for the temperature difference between the asphalt and the ambient based on the thermal circuit is

$$T_{asphalt} = \frac{\left(\frac{1}{2}R_a + R_c\right)\left(\frac{1}{2}R_a + R_{am}\right)}{R_a + R_c + R_{am}}Q_{in}. \tag{5}$$

This temperature difference is independent on the area A that is used. Therefore it is a useful characteristic for a highway where the thickness of the layers are defined. To set an upper limit for permissible heating of IHA, temperature difference between the ambient and the asphalt is set to be 5 °C then power density q_{in} in the IHA layer is

$$\begin{aligned} Q_{in,max} &= \frac{R_a + R_c + R_{am}}{\left(\frac{1}{2}R_a + R_c\right)\left(\frac{1}{2}R_a + R_{am}\right)}T_{a,max}\ [\mathrm{W}] \\ q_{in,max} &= \frac{Q_{in,max}}{Ax_a}\ [\mathrm{W\,m^{-3}}] \\ &= 2.38\ \mathrm{kW\,m^{-3}} \end{aligned} \tag{6}$$

2.2. Loss model of combined inductive system

In case of an IPT system, to transfer a large amount of power efficiently, capacitive compensation is carried out in both the primary and secondary. This technique nullifies reactive power and enhances power delivered to a load. Many combinations of capacitors in series and parallel yield several IPT compensation topologies. Due to a lack of standard coil definitions for EV IPT studies thus far, researchers build coils of various shapes and sizes that suite their requirements. Hence, to obtain specific results in all experimentation, the authors have considered coupling coefficient (dimensionless parameter) as the base metric. A combined IPT and IHA system will have additional losses inside the asphalt due to the alternating magnetic field, which is represented in the equivalent circuit as a series resistance as shown in Fig. 6.

Herein, the resistances $R_{1,\mathrm{field}}(\omega)$ and $R_{2,\mathrm{field}}(\omega)$ represent the frequency dependent induced losses inside the asphalt due to the fields created by the primary and secondary coils respectively, while resistance R_{M} represents the losses that are due to the combined field of the primary and secondary coils.

The coil voltages represented as vector $\mathbf{V}$ is related to coil currents $\mathbf{I}$ by (7),

$$\mathbf{V} = \begin{bmatrix} R_1(\omega) & R_{\mathrm{M}}(\omega) \\ R_{\mathrm{M}}(\omega) & R_2(\omega) \end{bmatrix}\mathbf{I} + j\omega\begin{bmatrix} L_1 & M \\ M & L_2 \end{bmatrix}\mathbf{I} \tag{7}$$

where L_1 and L_2 are self inductances of the primary and secondary coils, with M as mutual inductance respectively and the corresponding resistances R_1 and R_2, related to the dc coil resistances ($R_{1,\mathrm{coil}}$,$R_{2,\mathrm{coil}}$) and given by (8),

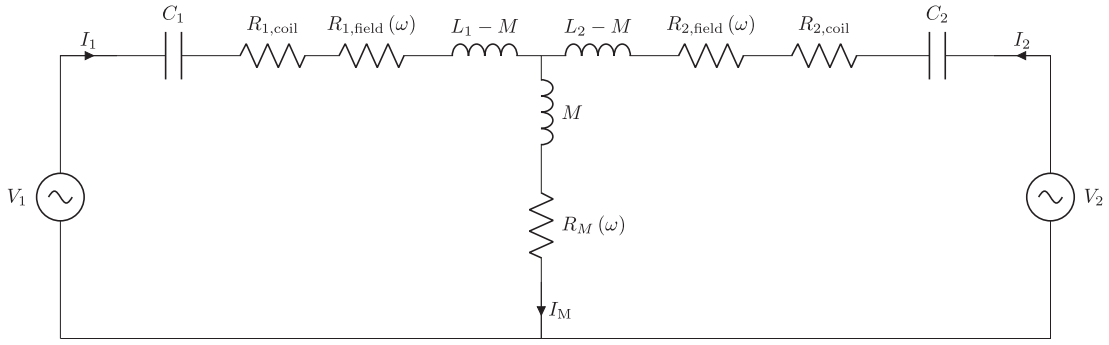

Fig. 6. Equivalent circuit of an IPT system including associated IHA losses. Series capacitors are shown as an illustration of reactive power compensation.

$$R_1(\omega) = R_{1,\text{coil}} + R_{1,\text{field}}(\omega)$$
$$R_2(\omega) = R_{2,coil} + R_{2,\text{field}}(\omega) \quad (8)$$

2.2.1. System performance

In order to compare the IPT system performance with and without IHA, the maximum possible efficiency $\eta_{\max}$ and the coupling factor k are used. The uncompensated power transfer (without capacitors) is used in this paper to decouple the power transfer from different types of compensation that can be used. Furthermore, the addition of compensation only scales the uncompensated power by the loaded quality factor of the secondary further justifying the use of uncompensated power as a system parameter. The $\eta_{\max}$ is derived from the maximum output apparent power $S_{\text{out,max}}$ using the same logical evolution in [20] with the assumption that primary and secondary leakages are compensated by the capacitances and is given by (9),

$$S_{\text{out,max}} = V_{\text{out,oc}} I^*_{\text{out,sc}} \quad (9)$$

where $V_{\text{out,oc}}$ is the open circuit output voltage and $I_{\text{out,sc}}$ is the short circuit output current. Now, the expression for $S_{\text{out,max}}$ is derived and given by (10)

$$V_{\text{out,oc}} = (R_M + j\omega M) I_1$$
$$I_{\text{out,sc}} = \frac{(R_M + j\omega M)}{R_2} I_1$$
$$S_{\text{out,max}} = \frac{R_M^2 + \omega^2 M^2}{R_2} I_1^2 \quad (10)$$

The maximum output power is related to this uncompensated apparent power as, $P_{\text{out,max}} = S_{\text{out,max}}$. Also, the input power that drives this output is given by (11).

$$P_{\text{in,min}} = R_1 I_1^2 + P_{\text{out,max}} \quad (11)$$

From (10) and (11), maximum efficiency can be derived as (12),

$$\eta_{max} = \frac{R_M^2 + \omega^2 M^2}{R_1 R_2 + R_M^2 + \omega^2 M^2}. \quad (12)$$

2.3. Numerical analysis

FEM analysis of a combined IPT and IHA system is performed in a 2-d environment with axial-symmetry in Comsol Multiphysics 5.1 over a range of frequencies from 1 kHz to 1 MHz. The geometry that is used has a circular primary coil of 26 turns with a wire radius of 1.1 mm, an inner radius of 37 mm and an outer radius of 105 mm. The secondary is

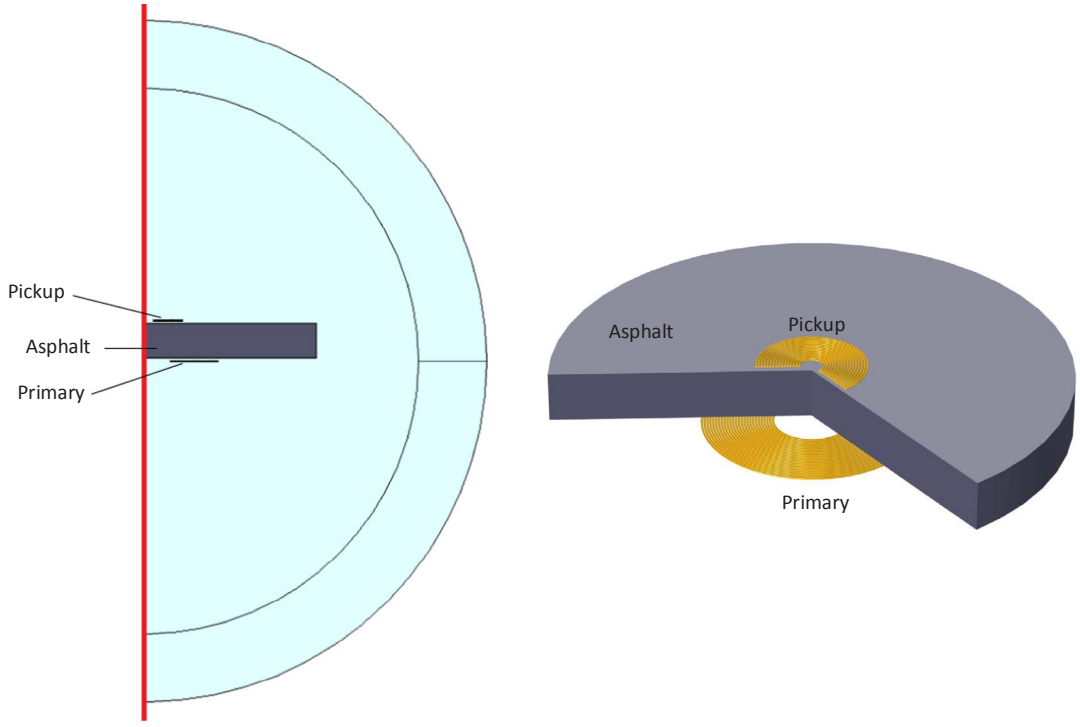

Fig. 7. Developed 2-d axis-symmetrical model and a 3-d overview model of the combined IPT and IHA system.

a circular coil of 16 turns with a wire radius of 1.1 mm, an inner radius of 12 mm and an outer radius of 53 mm. These dimensions are chosen to make a scaled-down laboratory experimental setup that can be used with the sample of IHA made available. The vertical offset between the primary and the asphalt layer is 5 mm, and the offset between the asphalt and the secondary is 20 mm. The radius of the asphalt layer is 250 mm and the layer is 50 mm thick. The numerical model developed is shown in Fig. 7.

2.3.1. Parameter extraction

The parameters for the equivalent circuit of Fig. 6 are extracted from the results of FEM analysis. For each coil, the parameters are extracted using the emf vector (for both coils) $\mathcal{E}$, currents vector $\mathbf{I}$ and power P from the simulations. The induced emf in the coils is given by

$$\mathcal{E} = j\omega \begin{bmatrix} L_1 & M \\ M & L_2 \end{bmatrix} \mathbf{I} \tag{13}$$

First, the self-inductance of the primary coil L_1 is calculated by exciting the coil while the secondary is simulated as an open circuit. The emf becomes

$$\begin{bmatrix} \mathcal{E}_1 \\ \mathcal{E}_2 \end{bmatrix} = j\omega \begin{bmatrix} L_1 & M \\ M & L_2 \end{bmatrix} \begin{bmatrix} \mathbf{I}_1 \\ 0 \end{bmatrix}, \tag{14}$$

from this, L_1 can be calculated as

$$L_1 = \frac{\mathcal{E}_1}{j\omega \mathbf{I}_1}. \tag{15}$$

In the same way, the inductance of the secondary coil can be calculated. Now, to obtain the mutual inductance, the secondary coil is simulated as a short circuit while the primary is excited. Using the previously calculated self inductance L_1 and the current through secondary $\mathbf{I}_2$, an expression for the mutual inductance $M = k\sqrt{(L_1 L_2)}$ can be derived as

$$\begin{aligned} \mathcal{E}_1 &= j\omega L_1 \mathbf{I}_1 + j\omega M \mathbf{I}_2 \\ M &= \frac{\mathcal{E}_1 - j\omega L_1 \mathbf{I}_1}{j\omega \mathbf{I}_2}. \end{aligned} \tag{16}$$

2.3.2. Numerical analysis results

From the numerical analysis, the circuit parameters are extracted and the performance of the system is analyzed with maximum power transfer and the magnetic coupling factor. The combined IPT and IHA system is compared with an air core system in Fig. 8. The frequency of interest - 85 kHz which is earmarked in the upcoming standard SAE J2954 for roadway IPT EV systems. At 85 kHz, the maximum efficiency of the combined system drops to 93%. It can also be seen that the coupling factor is lower than that of air-cored coils and start decreasing rapidly from 100 kHz. The coupling regime for the experimental IPT system is $k = 0.113$ and IHA sample volume is $8.84 \times 10^{-3}\,\mathrm{m}^3$. The coupling is now reduced to $k_{IHA} = 0.107$.

Further analysis is carried out with variable asphalt layer thickness. The chosen thickness's of the layer is 10 mm, 50 mm and 100 mm. The coupling variations when these combinations are compared with air-cored IPT systems with regular asphalt and that of IHA is presented in Fig. 9. In the range of 1–10 kHz, the coupling remains unchanged for both standard asphalt and self-healing asphalt. In this range, the coupling with 1 cm of inductive healing asphalt is decreased to 69% of the conventional asphalt. As observed, there is a reduction in coupling with increasing thickness of IHA due to eddy currents induced in the IHA. This effect also increases with increasing frequency and asphalt

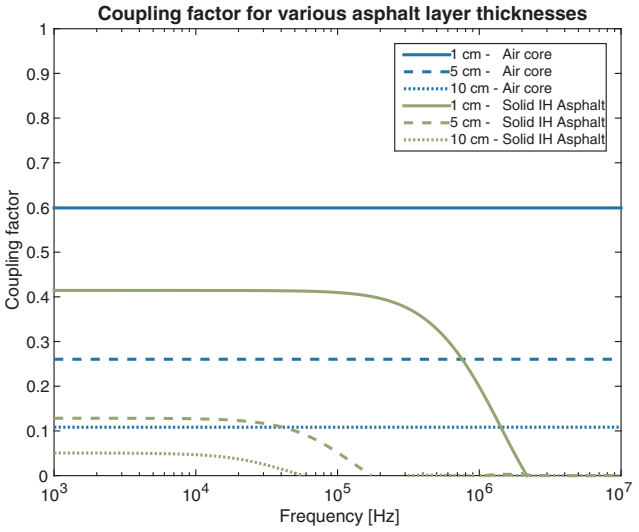

Fig. 9. Comparing coupling coefficients of air-cored IPT asphalt systems and IHA-IPT systems with variable asphalt thickness.

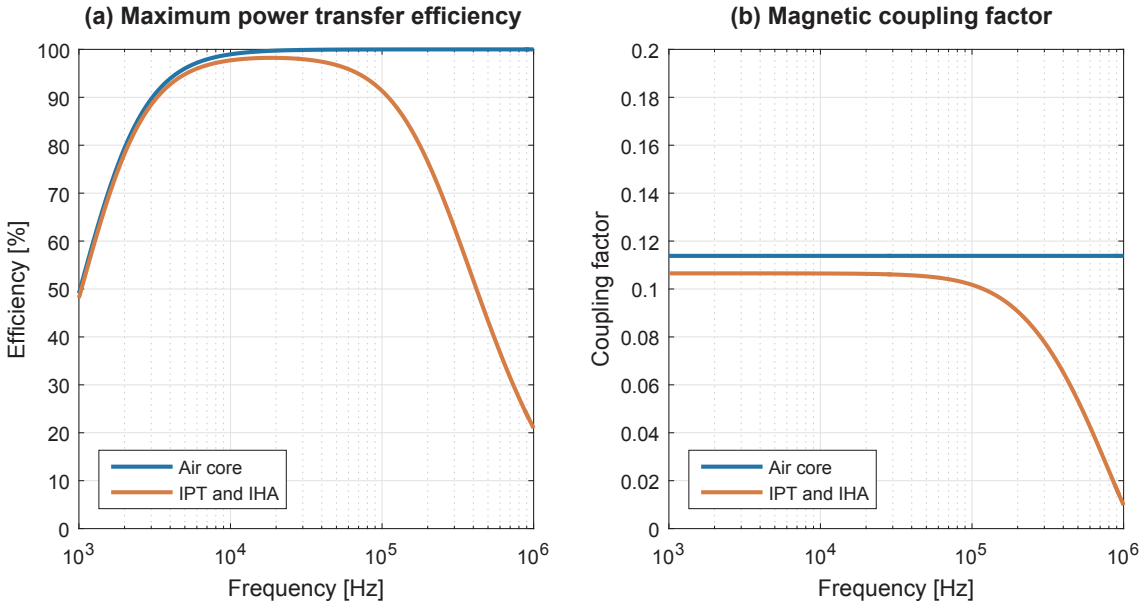

Fig. 8. Performance of a combined IPT and IHA system compared with an air core system. (a) Shows the maximum efficiency from the primary to the secondary and (b) shows the magnetic coupling factor between the primary and secondary.

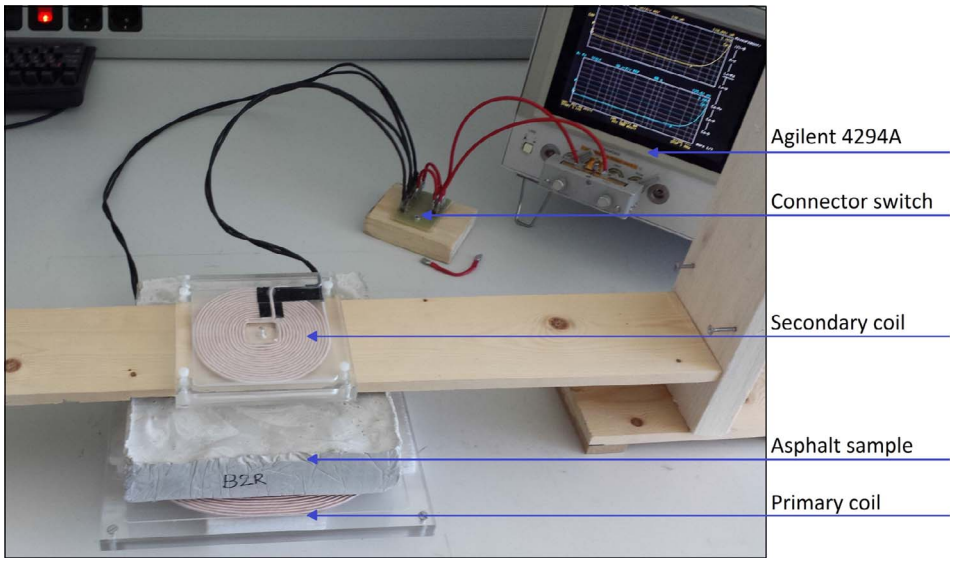

Fig. 10. Overview of the setup of the measurement of combined IHA-IPT with a rectangular block of asphalt.

thickness in IHA. Thus, there is considerable loss of power in the self-healing asphalt during energy transfer to EVs.

2.4. Experimental verification

The numerical results developed previously are verified with an experimental setup as shown in Fig. 10. The circuit parameters are measured with the Agilent 4294A Precision Impedance Analyzer. The geometry is the same as the system analyzed in the numerical evaluation, except that sample of asphalt is a square with sides of 200 mm. Therefore the numerical analysis is performed again with an asphalt layer radius of 113 mm, such that the volume of the cylindrical slab from the numerical evaluation is conserved as that of the experimental square block.

2.4.1. Parameter extraction

The circuit parameters are measured for a frequency range of 1 kHz to 1 MHz. For the mutual parameters, the primary and secondary coil are connected in series with a constructive flux addition (flux aiding). The measured impedance is then

$$Z_c = (R_1 + R_2 + 2R_M) + j\omega(L_1 + L_2 + 2M). \quad (17)$$

The measured impedance in destructive flux superposition is

$$Z_d = (R_1 + R_2 - 2R_M) + j\omega(L_1 + L_2 - 2M). \quad (18)$$

The mutual parameters can now be calculated as

$$Z_m = \frac{Z_c - Z_d}{4} = R_M + j\omega M. \quad (19)$$

2.4.2. Experimental results

The measured circuit parameters are presented together with the numerical results in Fig. 11. The inductance values obtained from FEM simulations agree with the experimental results as shown in Fig. 11(a). The small difference observed is due to interconnection wires leading to the impedance analyzer and minor differences between the real and the simulated coils. The resistance values are presented in Fig. 11(b). In the experimental system, the coil losses are higher and are variable with frequency. The frequency dependence is because of skin effect and proximity effect in the coils and due to stray fields (conductive parts below the table of the setup). The field losses due to the asphalt sample are calculated by subtracting the air core system resistances from the resistances measured with the asphalt sample in between. For the low-frequency values, the expected losses are less than the accuracy (limited resolution of the impedance analyzer), thus they do not match exactly with the simulations. From 20 kHz, the losses are accurately measured with the result that field losses are consistent with simulations. There is a minor offset noticeable, and this is due to the square geometry of experimental asphalt and cylindrical geometry of simulation.

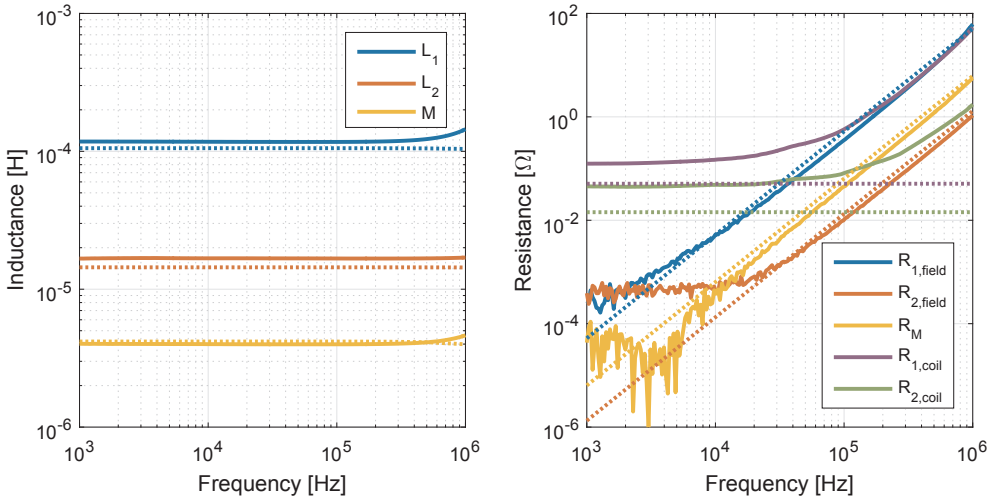

Fig. 11. Measured inductance and resistance values (solid line) of combined IPT and IHA plotted with respect to frequency and compared with the numerical results (dotted line).

2.4.3. Discussion

From the numerical analysis that is performed, it is clear there will be a reduction in efficiency and power transferred when IPT is combined with IHA. The reduction in efficiency and power transferred at 85 kHz can be a problem when the system operates at high power. This can lead to unintended asphalt heating. A further challenge is that the additional leakage in the system (due to IHA) can lead to variable tuning requirements for reactive power compensation. Finally, movement of cars will impact the energy transmission to the battery of EV from a fixed charge-pad in the ground. In addition, misalignment of the pick-up will impact the power transfer efficiency. These secondary effects have not been considered in this study.

One direction for a coexistence of the two technologies is based on the concept of sectional roads. Here, wheels of vehicles that are loading zones would result in enhanced raveling and damage of roads where they pass. On an average, the center of the roadway is subject to less stress. The zones along the sides where wheels move could be made of self-healing asphalt. On the other hand, the center of the road where energy transfer through IPT systems is necessary, standard asphalt can be paved. This way both healing and energy transfer are optimally utilized while sharing infrastructure. The same charge-pads could be used for both the operation by switching magnetic fields between the two zones. Further research is being carried out in this area also considering the material selection of IHA for asphalt roads wherein the healing process doesn't impact IPT while it serves IHA when required. Importantly, accurate modelling of the system is carried out.

3. Integration of solar roads with IPT charging

The integrated system consists of an IPT system with solar road sand witched in between. In order to obtain empirical understanding of the magnetic coupling between IPT coils sandwiching a solar road element in between, a lab scale prototype is tested.

Fig. 12 shows the experimental setup of the IPT coils with 17 cm air gap, Case (a) without solar cell in between, Case (b) with SR in between. Measurements for mutual inductance are conducted on IPT coils, first without, then with the solar cell following the methodology presented in Section 2.4.1. The frequency dependent mutual inductance is calculated from the measured values using (19) and converted to coupling. Fig. 13 shows the measured coupling between the IPT coils for different operating frequencies for each case.

It is observed the coupling starts decreasing linearly after 10 kHz on a logarithmic frequency scale. Considering that the desired operating frequency of the IPT system would be around 85 kHz, this decrease in the coupling of ≈50% leads to a reduction in efficiency as well as the cost of charging infrastructure for the same power level. For frequencies higher than 10 kHz, the decrease in mutual inductance is hypothesized due to the eddy currents in the conductive parts of the solar road element. Specifically, in the frequency range of 85 kHz, the coupling of the coils fall from $k = 0.022$ to $k = 0.0135$.

To prove the validity of these inferences, numerical FEM analysis is carried out using COMSOL and the model developed is shown in Fig. 14. Both the coils are of 50 turns each with an air gap of 17 cm and radius of 0.5 m. The primary coil is energized with 1 A current for frequencies 1 Hz, 100 Hz, 1 kHz, 10 kHz and 100 kHz. In the simulations, a thicker 10 mm aluminium back surface is considered for the solar cell for adequate computational capability and removing the influence of skin effect, which comes into effect at frequencies lower than 10 kHz. This frequency range is much lower than the operational regime of the IPT system.

Each solar cell is of 156 × 156 mm^2. A side view of the model is shown in Fig. 14(b). The eddy currents will be generated mainly in the metallic back contact of the solar cell. 10 mm thick aluminium layer is defined while the semiconductor layers are neglected in the analysis (due to several order lower conductivity). The surface plot of induced eddy currents in the solar road when primary IPT coil is excited with

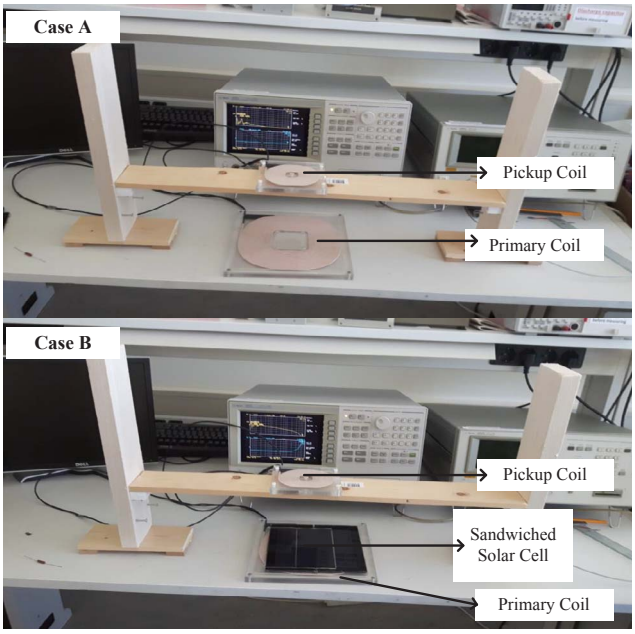

Fig. 12. Experimental setup for solar road element in combination with IPT charging coils.

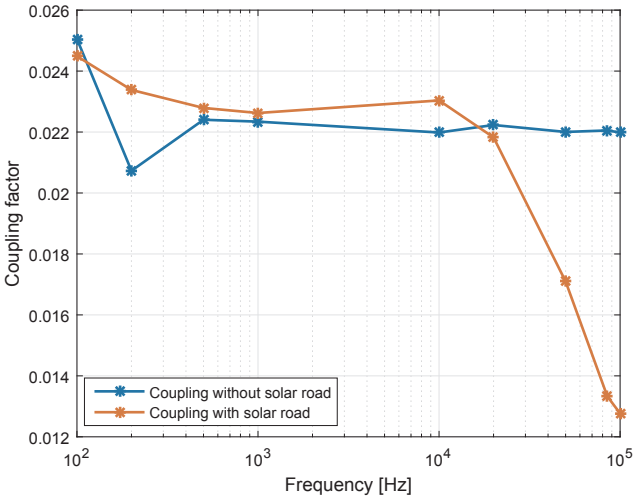

Fig. 13. Measured coupling and frequency with the introduction of solar road element. As the frequency increases beyond 10 kHz, the eddy currents begin to dominate and coupling decays exponentially in case of the solar road.

1 A current at 50 Hz is shown as an example in Fig. 15.

The red[1] arrows depict the coil current direction while the black arrows show the direction of opposing induced currents. Apart from eddy current, a frequency dependant decrease in the mutual inductance is observed. The mutual inductance between the IPT coils is calculated using (20).

$$M = \left(\frac{N_{\text{primary}}}{N_{\text{pickup}}}\right)\left(\frac{V_{\text{pickup}}}{j\omega I_{\text{primary}}}\right) \tag{20}$$

In the model, the primary and pick up turns are 50, while the induced voltage in the pickup coil (V_{pickup}) is simulated for different frequencies. The mutual inductance for different operating frequencies of IPT system with and without solar cell in between is shown in Fig. 16.

It can be observed that at the operating frequency increases, the

[1] For interpretation of color in 'Fig. 15', the reader is referred to the web version of this article.

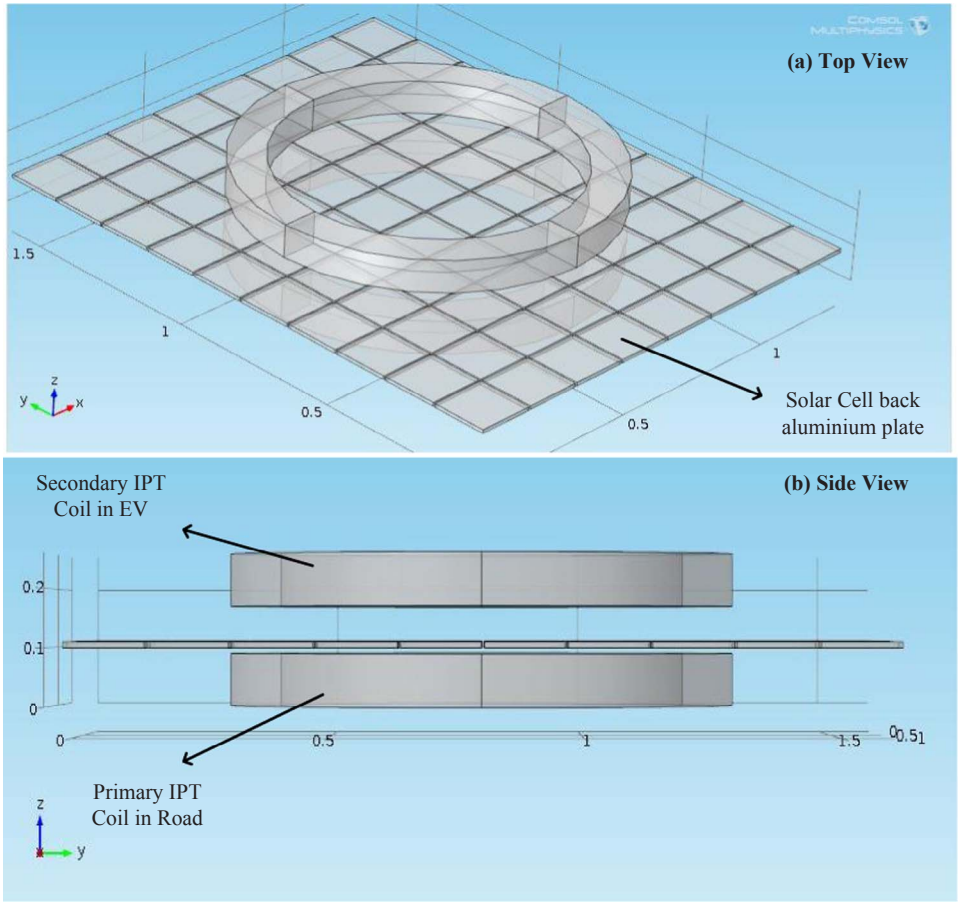

Fig. 14. COMSOL model for validating the inferences of the experimental results.

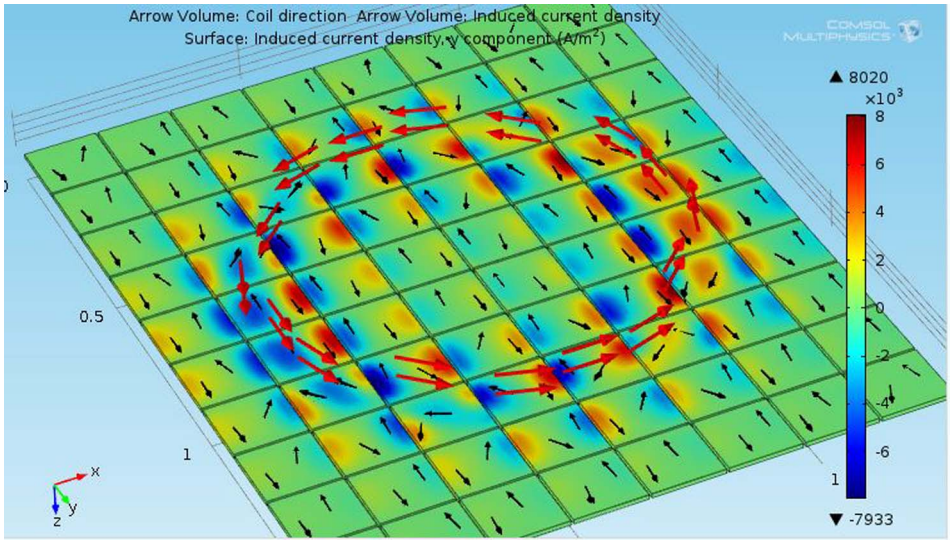

Fig. 15. Eddy currents induced in the solar road at 50 Hz.

mutual inductance decreases. The thickness of aluminium back contact is taken as 10 mm in this simulation. In actual practice, the solar road itself, and hence its back contact is a fraction of this thickness. Therefore, mutual inductance would start reducing only after 10 kHz due to skin effect, which plays a positive role in our application, as observed in experimental results of Fig. 13. Nevertheless, skin effect is not effective in limiting the eddy currents for IPT operating frequencies of 85–100 kHz. Therefore, the power transfer capability significantly reduces with lower mutual coupling. Further, the efficiency of IPT operation drops due to heating losses in the solar cell back contact due to these eddy currents.

3.1. Discussion

Based on the understanding derived from the theoretical and experimental study in this section, the following conclusions are drawn:

- It is recommended that the solar road is installed in the emergency lane of the highway. Not only will this avoid proximity with the on-road IPT charging, but also reduce dynamic shading of the solar cell

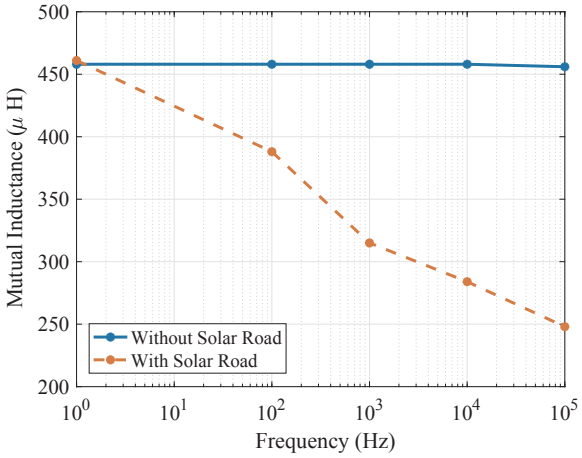

Fig. 16. Decreasing mutual inductance between IPT coils as a function of operating frequency in the finite element model.

by passing vehicles. Also, emergency lanes usually have low occupancy and now, energy utilization is made feasible.

- If dynamic IPT charging is not required for complete highways coverage [40], a Mosaic on-road space sharing design instead of sandwiched structure can be used.
- From a solar cell design point of view, an ultra-thin or meshed instead of a sheet of metallic back contact could reduce the eddy current. Smaller unit cells could also be advantageous. However, these possibilities and their consequences on the solar road performance are beyond the scope of this paper.

4. Case-study of a future highway

For the design of future highway with IPT, green energy, solar road and self-healing properties, the A12 motorway in Netherlands is used as a test case, shown in Fig. 17. A12 highway is 165 km and connects the city of Hague and Arnhem in Netherlands. For the design, a Nissan Leaf EV with 24 kW h battery pack is used as a reference and is assumed that the battery has an 85% efficiency. Such an EV represents a worst-case scenario for driving range due to its limited battery capacity as compared to EV with a much larger battery pack like the Tesla Model S with 85 kW h.

4.1. Design of IPT system for A12

Of the total 165 km, it is assumed that the EV drives 10 km each at the beginning and end of the highway in the urban areas at 60 km/h and the remaining 145 km at the speed limit of 120 km/h. The dynamics of the EV driving are simulated based on the model in [41]. The power demanded by the EV for driving is dependent on the speed of the EV. This can be linearly estimated as 5.6 kW when driving at a speed of 60 km/h and goes up to 24.1 kW for 120 km/h speed. Based on this, it has been estimated that the required energy for the Leaf to cover 165 km is 31 kW h [38]. This value is higher than the 24 kW h capacity of the Leaf even if it is assumed that the EV begins at 100% SOC and ends the journey at 0% SOC, which never occurs practically.

In order to ensure that the EV is able to comfortably complete the journey without having to stop, the IPT system is used to charge it enroute. The motive of the IPT system is that if an EV begins the journey with 80% SOC, it must complete the trip along A12 with at least a SOC of 20%. This corresponds to using 24 kW h × (80%−20%) × 85% = 12.2 kW h of the EV battery at 85% round-trip efficiency. The remaining (31–12.2) = 18.8 kW h has to be supplied by the IPT. To achieve this, a 50 kW IPT system with 85% efficiency is used. This value is based on actual measurements reported in [42] and using a conservative estimate of the expectations from dynamic charging [43]. To meet the energy demand, the IPT system has to be installed over a length of 50 km [38]. This IPT is assumed to be installed in the busiest parts of the highway indicated as A and B in Fig. 17.

The SOC of the battery along the highway as the EV drives from Hague to Arnhem is shown in Fig. 18. Without an IPT system, the SOC reduces from 80% and EV runs out of energy by the time it has crossed 96 km. With the IPT system, the EV is able to fulfill the full length of 165 km with a SOC of 20–25% remaining. If the EV travels at an average speed lower than 120 km/h which happens most of the time in practice, then it finishes the journey with a higher SOC as shown in Fig. 18 for speeds of 110 km/h and 100 km/h. This demonstrates the effectiveness of using IPT for on-road charging of EVs.

Economic analysis of dynamic IPT system for on-road charging was performed in [40]. The designed system had 200 kW rated power at a specific cost of 1.2 M€/km/lane. Considering 0.1 M€/km of constant road construction costs, the specific cost of a scaled-down system of 50 kW would be 0.375 M€/km/lane, resulting in a system cost of 37.5 M€for 50 km two-lane coverage.

4.2. Powering the IPT system using renewables

In 2030, 2.3 million electric vehicles are expected in the Netherlands which comprises about 40% of all cars. For calculations on the power demand, it is assumed that 10% of all EV will charge while driving using the IPT system. This assumption is based on balancing the pressures between the maturity of IPT technology and the cost of upgrading infrastructure. The combined power demand of the EV per hour for a round trip on A12 is shown in Fig. 19. The peak demand reaches 18 MW in the evening while the lowest demand is less than 1 MW in the early mornings.

To have a truly sustainable IPT system, this energy required by the EV must be powered from renewable sources. This can be achieved by the use of solar roads, wind turbines and vortex turbines along the A12 highway. Since there is variability in the renewable generation on a diurnal and seasonal basis, the motive here would be to supply the energy required by the IPT system on an yearly basis in an energy neutral manner. This means the grid is used as an energy buffer to manage the variability in generation.

The total length of these lanes on the A12 is 114 km. The surface of this lane on both sides of the road which can generate solar energy is 2 × 114 km × 3.5 m = 0.798 km^2. The efficiency of the solar road is 9.69% [34]. The practical effects of dynamic shading – dust/dirt, shadow from buildings, etc. will reduce the efficiency and energy harvested, these effects are not considered in this study. The energy that can be generated per day using the solar road for different months of the year has been estimated and shown in Fig. 20. It can be seen that the energy generation varies from 350 MW h in summer to 50 MW h in winter. The 114 km solar road can provide for 95% of the energy requirements of the IPT over the year with a surface of 0.789 km^2.

According to the estimates of the current solar road installation, it cost 3 M€for 175 m^2 area including power electronics, panels, road costs and installation. Assuming a 40% reduction in cost as the technology matures, the solar road would cost 9576 M€for the 114 km stretch, as

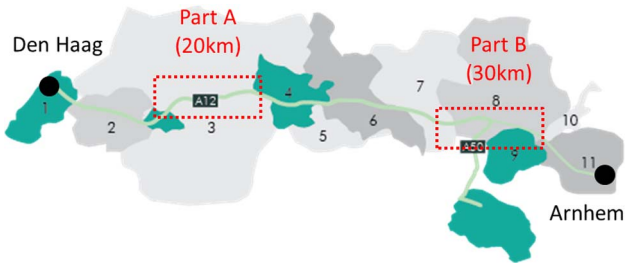

Fig. 17. A12 highway between Den Haag and Arnhem with IPT system installed over two section – Part A for 20 km and Part B for 30 km.

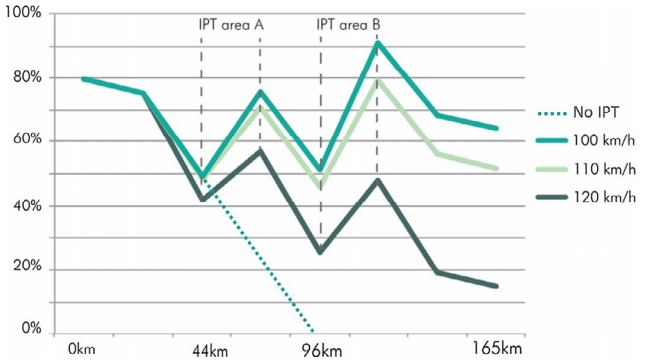

Fig. 18. The SOC of the battery along the A12 highway for different driving speeds. The average speed for urban driving remained the same for all three situations. A driving speed of 100 km/h is more energy efficient.

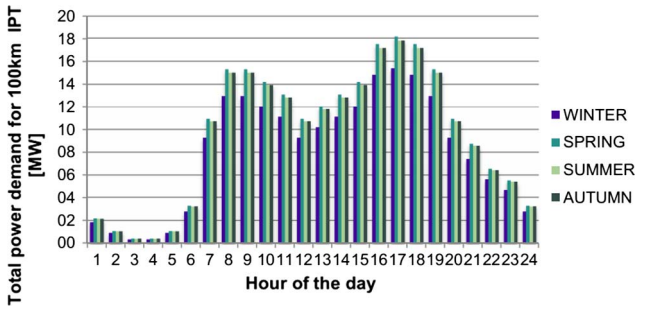

Fig. 19. Seasonal dependence of power demand of IPT powered EVs per hour for a round trip on A12.

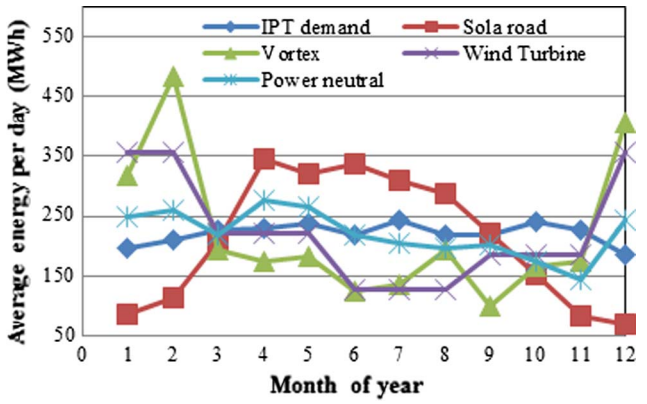

Fig. 20. Average energy generated per day by renewables to power the IPT system on A12. Both emergency lanes are replaced with a solar road and wind turbines and vortex are used to extract power from the wind.

Table 2
Energy mix for powering the IPT using renewables.

Case	Vortex 4 kW	WT 2 MW	SR %	Energy Neut. %
SR	0	0	100	95.5
Vortex	14860	0	0	100
WT	0	107	0	100
SR + Vortex	7775	0	50	100
SR + WT	0	56	50	100
Power Neutral	0	64	42	100

shown in Table 2. For harnessing wind power, two types of wind turbines are considered. First is a 2 MW conventional wind turbines with a minimum speed of 4 m/s. Second, a 4 kW Vortex mini wind turbines operating at a rated speed of 12 m/s and minimum speed of 2 m/s. The wind generation trend is opposite to solar road showing higher generation in winter and lesser in summer as shown in Fig. 20.

The cost of the wind turbine are estimated in Table 3 based on [44] and cost of the vortex is estimated by the manufacturer to be 50% lower than conventional wind turbines. This lower cost is mainly owing to the lack of rotating turbine and simpler support system.

Based on the operating characteristics of the two turbines and meteorological data from the KNMI, 14860 vortex or 107 wind turbines would be required to produce enough energy to 100% match with the energy requirements of the IPT as shown in Fig. 20 and Table 2.

The vortex is the cheapest renewable source costing 59.44 M€for installation. The operating and maintenance costs of the vortex and turbine have not been considered in the analysis where the vortex is expected to have 50% and 80% lower costs for each respectively. However, it is important to mention that vortex is an early stage innovation and the cost and performance used in the analysis are subject to change.

Table 2 also estimates the number and cost of the wind generators required when the solar road coverage is reduced by half to 57 km. In [45], it is obtained that a 40–60% combination of solar and wind is most ideal in achieving power neutral generation in Netherlands where the higher generation of solar in summer and in the day is balanced by the higher generation of wind in the night and in winter. It can be seen in Fig. 20, that the combination of wind and solar gives a generation that closely follows the IPT demand for different months of the year.

5. Conclusion

In this paper, functional integration of different elements of future highways has been analyzed, along with a system level study of a real-highway implementation in the Netherlands.

Sharing of infrastructure for both IPT and IHA is important for future highways. A thermal model with power densities for healing and maximum permissible limit to prevent raveling is proposed. A loss model that integrates eddy current losses by utilizing frequency-dependent resistances are included in this paper. The challenge in this integration is that up to a frequency of 100 kHz, the magnetic efficiency and power transfer of IPT systems drops to 90% in the coupling regime of $k = 0.113$ for 5 cm IHA. Thus, direct integration can be lossy. Further work is being carried out in the use of a frequency decoupled material optimization, thereby sharing the IPT and IHA magnetics (power electronics and coils) and using an earmarked frequency for power transfer and another for healing. Sectional roadways with magnetic field for energy transfer along the center and inductive healing asphalt along load centers at the edges is one such possibility. The idea for such a combination, with no interference between the two technologies, is the result of learning from the integration challenges as attempted in this paper.

Solar roads and IPT system, placed closeby would result in lower transmission losses due to in situ energy generation and utilization. A sandwich approach couldn't work due to eddy currents induced in the backplates of the solar roads. The coupling declined to $k = 0.0135$, a reduction of 38.6% at operation close to 85 kHz. It is therefore considered to use emergency lanes of roads for solar roads operation. In the

Table 3
Estimation of cost of the 2 MW wind turbine and 4 kW vortex.

	2 MW WT €/kW	4 kW vortex €/kW
Grid connection (11%)	220	220
Foundation (16%)	320	140
Turbine (64%)	1280	560
Planning (9%)	180	80
Costs	2000	1000
Total cost	4000 k€	6.66 k€

proposed energy conversion highway model, it is shown that a Nissan LEAF can complete its trip with 80–25% SOC along highway A12 with on-road IPT system enabled. The total IPT coverage (assumed IPT efficiency = 85%) in this highway is 30.3%. This corresponds to a distance of 50 km in a highway of total length 165 km. In the Netherlands, due to the complementary distribution of wind-solar profiles (peaks in winter and summer respectively), the choice of solar and wind technologies must match with the overall availability of renewable energy. The cost comparison of a 2 MW conventional wind turbine and 4 kW vortex results in a total cost of 4000 k€/kW and 6.66 k€/kW respectively. While vortex is cost-effective, it is still an experimental technology and hence an optimal mix of different technologies would be the best techno-economic scenario.

The experimental lab-scale prototypes developed for each technology shows the potential application in optimal roadway infrastructure and energy utilization. Increasing interest in the individual development of such solutions that current trends indicate is, therefore, not unexpected. However, this study emphasizes that increasing integration of such components would inevitably lead to challenges and some feasible alternatives. These possibilities are showcased using both theoretical computations and experiments. In conclusion, a multidisciplinary approach would not only help mitigate these issues, but could possibly offer some exciting opportunities in maximizing the benefits such combined integration could bring for emerging technologies toward sustainable roadways.

Acknowledgments

The authors wish to acknowledge the contributions of Nederlandse Organisatie voor Toegepast Natuurwetenschappelijk Onderzoek (TNO) and Stan Klerks (TNO) for their work on solar roads. Also, the authors wish to thank prof. Erik Schlangen (CiTG, TU Delft) and Dr. Amir Tabakovic for their work in the development of self-healing roads.

References

[1] Dijk M, Orsato RJ, Kemp R. The emergence of an electric mobility trajectory. Energy Policy 2013;52:135–45. http://dx.doi.org/10.1016/j.enpol.2012.04.024 < http://linkinghub.elsevier.com/retrieve/pii/S0301421512003242 > .

[2] Ajanovic A, Haas R. Dissemination of electric vehicles in urban areas: major factors for success. Energy 2016;115(Part 2):1451–8. http://dx.doi.org/10.1016/j.energy.2016.05.040. [towards low carbon energy systems: engineering and economic perspective]. < http://www.sciencedirect.com/science/article/pii/S0360544216306508 > .

[3] Lutsey N. Global climate change mitigation potential from a transition to electric vehicles; 2015.

[4] Mouli GC, Bauer P, Zeman M. System design for a solar powered electric vehicle charging station for workplaces. Appl Energy 2016;168(Suppl C):434–43. http://dx.doi.org/10.1016/j.apenergy.2016.01.110 < http://www.sciencedirect.com/science/article/pii/S0306261916300988 > .

[5] Ombach G, Kurschner D, Mathar S. Universal base coil solution for interoperable system for stationary wireless ev charging. In: 2015 International conference on sustainable mobility applications, renewables and technology (SMART); 2015. p. 1–9. http://dx.doi.org/10.1109/SMART.2015.7399238.

[6] Covic GA, Boys JT. Inductive power transfer. Proc IEEE 2013;101(6):1276–89. http://dx.doi.org/10.1109/JPROC.2013.2244536 < http://ieeexplore.ieee.org/document/6492113/ > .

[7] Prasanth V, Bauer P. Distributed IPT systems for dynamic powering: misalignment analysis. IEEE Trans Ind Electron 2014;61(11):6013–21. http://dx.doi.org/10.1109/TIE.2014.2311380 < http://ieeexplore.ieee.org/lpdocs/epic03/wrapper.htm?arnumber=6766205 > .

[8] Carretero C. Coupling power losses in inductive power transfer systems with Litz-wire coils. IEEE Trans Ind Electron 2017;64(6):4474–82. http://dx.doi.org/10.1109/TIE.2017.2668988 < http://ieeexplore.ieee.org/document/7855720/ > .

[9] Mi CC, Buja G, Choi SY, Rim CT. Modern advances in wireless power transfer systems for roadway powered electric vehicles. IEEE Trans Ind Electron 2016;63(10):6533–45. http://dx.doi.org/10.1109/TIE.2016.2574993 < http://ieeexplore.ieee.org/document/7491313/ > .

[10] Budhia M, Covic GA, Boys JT. Design and optimization of circular magnetic structures for lumped inductive power transfer systems. IEEE Trans Power Electron 2011;26(11):3096–108. http://dx.doi.org/10.1109/TPEL.2011.2143730.

[11] Kim M, Byeon J, Lee BK, Lee JW. Performance analysis of magnetic power pads for inductive power transfer systems with ferrite structure variation. In: 2016 IEEE energy conversion congress and exposition (ECCE); 2016. p. 1–6. http://dx.doi.org/10.1109/ECCE.2016.7855338.

[12] Villa JL, Salln J, Llombart A, Sanz JF. Design of a high frequency inductively coupled power transfer system for electric vehicle battery charge. Appl Energy 2009;86(3):355–63. http://dx.doi.org/10.1016/j.apenergy.2008.05.009 < http://www.sciencedirect.com/science/article/pii/S0306261908001359 > .

[13] Venugopal P, Bandyopadhyay S, Bauer P, Ferreira JA. A generic matrix method to model the magnetics of multi-coil air-cored inductive power transfer systems. Energies 2017;10(6).

[14] Zhao L, Ruddell S, Thrimawithana DJ, Madawala UK, Hu PA. A hybrid wireless charging system with DDQ pads for dynamic charging of EVs. In: 2017 IEEE PELS workshop on emerging technologies: wireless power transfer (WoW); 2017. p. 1–6. http://dx.doi.org/10.1109/WoW.2017.7959397.

[15] Lin FY, Kim S, Covic GA, Boys JT. Effective coupling factors for series and parallel tuned secondaries in IPT systems using bipolar primary pads. IEEE Trans Transport Electrificat 2017;3(2):434–44. http://dx.doi.org/10.1109/TTE.2017.2648123.

[16] Zaheer A, Covic GA. A comparative study of various magnetic design topologies for a semi-dynamic EV charging application. In: 2016 IEEE 2nd annual southern power electronics conference (SPEC); 2016. p. 1–6. http://dx.doi.org/10.1109/SPEC.2016.7846203.

[17] Stamati TE, Bauer P. On-road charging of electric vehicles. In: 2013 IEEE transportation electrification conference and expo (ITEC); 2013. p. 1–8. http://dx.doi.org/10.1109/ITEC.2013.6573511.

[18] Fuller M. Wireless charging in california: range, recharge, and vehicle electrification. Transport Res Part C: Emerg Technol 2016;67(Suppl C):343–56. http://dx.doi.org/10.1016/j.trc.2016.02.013 < http://www.sciencedirect.com/science/article/pii/S0968090X16000668 > .

[19] Chopra S, Bauer P. Driving range extension of EV with on-road contactless power transfer – a case study. IEEE Trans Ind Electron 2013;60(1):329–38. http://dx.doi.org/10.1109/TIE.2011.2182015 < http://ieeexplore.ieee.org/document/6117077/ > .

[20] Covic GA, Boys JT. Modern trends in inductive power transfer for transportation applications. IEEE J Emerg Sel Top Power Electron 2013;1(1):28–41. http://dx.doi.org/10.1109/JESTPE.2013.2264473 < http://ieeexplore.ieee.org/document/6517868/ > .

[21] Voskuilen JLM, Verhoef PNW. Cause of premature raveling failure of porous asphalt. Sixth international RILEM symposium on performance testing and evaluation of bituminous materials 2003:191–7.

[22] Liu Quantao, Schlangen Erik, García Álvaro, van de Ven Martin. Induction heating of electrically conductive porous asphalt concrete. Constr Build Mater 2010;24(7):1207–13. http://dx.doi.org/10.1016/j.conbuildmat.2009.12.019. < http://www.sciencedirect.com/science/article/pii/S0950061809004309 > . ISSN 0950-0618.

[23] Little DN, Bhasin A. Self healing materials: an alternative approach to 20 centuries of materials science. Dordrecht: Springer Netherlands; 2007. p. 205–18 [chapter Exploring Mechanism of Healing in Asphalt Mixtures and Quantifying its Impact].

[24] Kim B, Roque R. Evaluation of healing property of asphalt mixtures. Transport Res Rec: J Transport Res Board 2006;1970:84–91.

[25] Liu Q. Induction healing of porous asphalt concrete. Ph.D. thesis. TU Delft; October 2012.

[26] Apostolidis P, Liu X, Scarpas A, Kasbergen C, van de Ven M. Advanced evaluation of asphalt mortar for induction healing purposes. Constr Build Mater 2016;126(Suppl C):9–25. http://dx.doi.org/10.1016/j.conbuildmat.2016.09.011 < http://www.sciencedirect.com/science/article/pii/S0950061816314404 > .

[27] Liu Q, García Á, Schlangen E, van de Ven M. Induction healing of asphalt mastic and porous asphalt concrete. Constr Build Mater 2011;25(9):3746–52. http://dx.doi.org/10.1016/j.conbuildmat.2011.04.016 < http://linkinghub.elsevier.com/retrieve/pii/S0950061811001565 > .

[28] Li X, Lopes LAC, Williamson SS. On the suitability of plug-in hybrid electric vehicle (PHEV) charging infrastructures based on wind and solar energy. In: 2009 IEEE power energy society general meeting; 2009. p. 1–8. http://dx.doi.org/10.1109/PES.2009.5275171.

[29] Qiao W, Sharma A, Hudgins JL, Jones EG, Rilett L. Wind/solar hybrid generation-based roadway microgrids. In: 2011 IEEE power and energy society general meeting; 2011. p. 1–7. http://dx.doi.org/10.1109/PES.2011.6039884.

[30] Stamati TE, Bauer P. Green energy for on-road charging of electric vehicles; 2012.

[31] Ramesh MV, Devidas AR, Rangan V. Using CPS enabled microgrid system for optimal power utilization and supply strategy. Energy Build 2017;145(Suppl C):32–43. http://dx.doi.org/10.1016/j.enbuild.2017.03.068. A.K. < http://www.sciencedirect.com/science/article/pii/S0378778816313901 > .

[32] Garca-Vzquez CA, Llorens-Iborra F, Fernndez-Ramrez LM, Snchez-Sainz H, Jurado F. Comparative study of dynamic wireless charging of electric vehicles in motorway, highway and urban stretches. Energy 2017;137(Suppl C):42–57. http://dx.doi.org/10.1016/j.energy.2017.07.016 < http://www.sciencedirect.com/science/article/pii/S0360544217311891 > .

[33] SolaRoad. < http://www.solaroad.nl/ > .

[34] Shekhar A, Klerks S, Bauer P, Prasanth V. Solar road operating efficiency and energy yield – an integrated approach towards inductive power transfer. In: Proceedings of the 31st European photovoltaic solar energy conference and exhibition, Hamburg; 14–18 Sept. 2015. Authors version. < https://repository.tudelft.nl/islandora/object/uuid%3Ab74a7682-1559-4c81-9a11-f77d1c5ac9e8 > .

[35] Vortex Bladeless. < http://www.vortexbladeless.com/ > .

[36] Bladeless wind turbines may offer more form than function – MIT technology review. < https://www.technologyreview.com/s/537721/bladeless-wind-turbines-may-offer-more-form-than-function/ > .

[37] Xiang B, Cao X, Yuan Y, Sun L, Wu H, Haghighat F. A novel hybrid energy system combined with solar-road and soil-regenerator: dynamic model and operational performance. Energy Convers Manage 2018;156:376–87. http://dx.doi.org/10.

1016/j.enconman.2017.11.066 < https://www.sciencedirect.com/science/article/pii/S0196890417311184 > .
[38] Prasanth V, Scheele N, Visser E, Shekhar A, Mouli GRC, Bauer P, et al. Green energy based inductive self-healing highways of the future. 2016 IEEE transportation electrification conference and expo (ITEC) IEEE; 2016. p. 1–8. http://dx.doi.org/10.1109/ITEC.2016.7520268 < http://ieeexplore.ieee.org/document/7520268/ > .
[39] der Zwan JV, et al. Porous asphalt wearing courses in the Netherlands a state of the art review; 2012.
[40] Shekhar A, Prasanth V, Bauer P, Bolech M. Economic viability study of an on-road wireless charging system with a generic driving range estimation method. Energies 2016;9(2):76. http://dx.doi.org/10.3390/en9020076 < http://www.mdpi.com/1996-1073/9/2/76 > .
[41] Shekhar A, Prasanth V, Bauer P, Bolech M. Generic methodology for driving range estimation of electric vehicle with on-road charging. 2015 IEEE transportation electrification conference and expo (ITEC) IEEE; 2015. p. 1–8. http://dx.doi.org/10.1109/ITEC.2015.7165763 < http://ieeexplore.ieee.org/document/7165763/ > .
[42] Zhou S, Mi CC. Multi-paralleled LCC reactive power compensation networks and their tuning method for electric vehicle dynamic wireless charging. IEEE Trans Ind Electron 2016;63(10):6546–56. http://dx.doi.org/10.1109/TIE.2015.2512236.
[43] Lukic S, Pantic Z. Cutting the cord: static and dynamic inductive wireless charging of electric vehicles. IEEE Electrificat Mag 2013;1(1):57–64. http://dx.doi.org/10.1109/MELE.2013.2273228.
[44] Renewable energy technology: cost analysis of wind power; 2012.
[45] Stamati TE, Bauer P. Green energy for on-road charging of electric vehicles. In: Proceedings of 15th international conference MECHATRONIKA; 2012. p. 1–9.